# Response of Humidity and Clouds to Tropical Deep Convection

Mark D. Zelinka and Dennis L. Hartmann

Department of Atmospheric Sciences
University of Washington
Seattle, WA

*Submitted to the*
Journal of Climate
30 January 2008

---

*Corresponding Author:* Mark D. Zelinka
Department of Atmospheric Sciences
University of Washington, Box 351640
Seattle, WA 98195
Email: mzelinka@atmos.washington.edu

**Abstract**

Currently available satellite data can be used to track the response of clouds and humidity to intense precipitation events. A compositing technique centered in space and time on locations experiencing high rain rates is used to detail the characteristic evolution of several quantities measured from a suite of satellite instruments. Intense precipitation events in the convective Tropics are preceded by an increase in low-level humidity. Optically thick cold clouds accompany the precipitation burst, which is followed by the development of spreading upper level anvil clouds and an increase in upper tropospheric humidity over a broader region than that occupied by the precipitation anomalies. The temporal separation between the convective event and the development of anvil clouds is about 3 hours. The humidity increase and associated decrease in clear-sky longwave emission persist for many hours after the convective event, even though the domain-averaged column integrated water vapor remains essentially constant over the composite period. Large-scale vertical motions from reanalysis show a coherent evolution associated with precipitation events identified in an independent dataset. Upward vertical motion anomalies associated with precipitation events begin with stronger upward motion anomalies in the lower troposphere, which then evolve toward stronger upward motion anomalies in the upper troposphere, in conjunction with the development of anvil clouds. Greater upper tropospheric moistening and cloudiness are associated with larger scale and better organized convective systems, but even weaker more isolated systems produce sustained upper level humidity and clear-sky OLR anomalies.

## 1. Introduction

Deep convective systems are prominent features of the tropical atmosphere that have important roles at a spectrum of space and time scales from local diurnal cycles to the planetary-scale Hadley and Walker circulations. Upward motion occurring in the ascending branches of the Hadley and Walker circulations is realized not in the form of large-scale continuous ascent but in the form of a large number of relatively small-scale discrete convective plumes occurring in an otherwise subsiding environment (Yanai et al. 1973). Because it is the ensemble of transient deep convective processes that results in the measured mean ascent in the Tropics, understanding the large spatial and long temporal scale tropical circulation requires understanding deep convective processes.

In addition to its dynamical importance for the tropical circulation, deep convection is the primary source of high clouds and free-tropospheric water vapor, which strongly impact the radiation budget of the planet. Stratiform anvil clouds that tend to have a negative net radiative forcing and thin cirrus clouds that tend to have a positive net radiative forcing (Hartmann, et al. 2001), spread outward from deep cumulonimbus clouds and are the most prominent cloud in the convective regions of the Tropics. Moist boundary layer air is transported by deep convection to the dry mid- and upper-troposphere, where even slight humidity increases can strongly reduce the radiation emitted to space (Shine and Sinha 1991; Udelhofen and Hartmann 1995; Spencer and Braswell 1996; Allan et al. 1999; Held and Soden 2000; Colman 2001). Because the ability of the Tropics to retain heat determines how much energy is available for export to the rest of the Earth (Pierrehumbert 1995), deep convection strongly affects not only the local radiation budget, but also the energy budget of the entire planet. Indeed, Soden and Fu (1995) find that the frequency of deep convection is strongly correlated with changes in upper tropospheric humidity, and that these variations are responsible for about half of the regional greenhouse effect variations. Several studies (Salathe and Hartmann 1997; Pierrehumbert and Roca 1998; Dessler and Sherwood 2000) demonstrate using trajectory analyses that transport of moisture away from deep convection is the primary mechanism by which the free troposphere is moistened, and that the sublimation of detrained condensate is not a significant moisture source. Inamdar and Ramanathan (1994) provide evidence for a super-greenhouse effect, in which the moistening effect of deep convection reduces the ability of the surface-atmosphere system to radiate away "excess" energy in regions of high SST.

The ability to properly simulate deep convection and the corresponding cloud and humidity fields remains a challenge to global climate models. Understanding how clouds and humidity will change under greenhouse warming is largely dependent on understanding the convective processes which determine their distribution, and this requires detailed measurements of tropical convective systems. In this study we use profiles of humidity retrieved by the Atmospheric Infrared Sounder (AIRS) and cloud properties from the Moderate Resolution Imaging Spectroradiometer (MODIS) onboard NASA's Aqua satellite to investigate the evolution of high clouds, humidity, and clear sky outgoing longwave radiation ($OLR_{CS}$) associated with deep convection. The spatial and temporal humidity and cloud distributions are investigated by compositing about locations of deep convection, identified by intense rain rates (RRs) from the Tropical Rainfall Measuring Mission (TRMM) Multisatellite Precipitation Analysis (TMPA). In addition, we assess the sensitivity of the upper tropospheric moisture and cloud evolution to the scale of the convection.

It is well known that while some tropical deep convection "pops up" in regions distant from synoptic support, the vast majority of deep convection is organized into convective complexes, which have been extensively documented (e.g., Houze and Betts 1981; Gamache and Houze 1983; Houze 1982; Chen and Houze 1997; Nuret and Chong 1998; Sherwood and Wahrlich 1999). These studies have largely relied on ground-based and geostationary satellite observations of individual convective systems during field campaigns. The present study aims to further detail the evolution of the moisture and cloud fields in the vicinity of tropical deep convective events throughout the tropical Pacific. We take a statistical approach as a means of showing climatological characteristics of convective systems rather than highly-detailed observations of individual systems.

The AIRS instrument is uniquely suited for measuring the humidity distribution: It provides radiosonde-quality humidity and temperature retrievals at high vertical resolution throughout the troposphere, unlike geostationary water vapor channels which sense vapor in a thick upper tropospheric layer between about 500 and 200 hPa; its global coverage allows observations from a broader range of locations than those within the radiosonde network or within field campaign domains; the duration of observations allow for a larger and more diverse set of samples than those of field campaigns; and the cloud-clearing techniques employed in the AIRS retrieval algorithm (Susskind et al. 2003) allow for sampling with greater confidence in cloudy regions where infrared retrievals from other instruments become contaminated.

## 2. Data and Quality Control

The Aqua satellite was launched on May 4, 2002 as part of NASA's Earth Observing System into a sun-synchronous near-polar orbit at 705.3 km above the earth's surface. The satellite ascends (descends) across the equator at approximately 1:30 PM (AM) local time providing global coverage approximately every two days, depending on the sensor. We use retrievals over the tropical Pacific ITCZ region (5°N to 15°N, 120°E to 260°E) between January 2003 and December 2005 from three sensors onboard Aqua: AIRS, MODIS, and AMSR-E. We also use a precipitation dataset (TMPA) that includes measurements from a suite of polar-orbiting and geostationary satellites. Finally we make use of horizontal and vertical winds from the NCEP/NCAR Reanalysis.

*a. AIRS*

The descriptions of the AIRS instruments are provided in detail in Aumann et al. (2003). AIRS is actually a suite of instruments, a hyperspectral infrared instrument (AIRS) with 2378 channels between 3.7 and 15.4 μm and a 13.5 km footprint at nadir, the Advanced Microwave Sounding Unit (AMSU-A) with 15 microwave channels between 23 and 90 GHz and a 40.5 km footprint at nadir, and a visible / near IR sensor with four channels between 0.40 and 0.94 μm and a 2.3 km footprint at nadir (Aumann et al. 2003). Within each AMSU-A field of view (FOV) is an array of three-by-three AIRS FOVs, and within each AIRS FOV is an array of eight-by-nine visible / near IR FOVs. The visible / near IR channels are primarily used to flag the presence of low clouds (Gautier et al. 2003). Because information from all sensors is used simultaneously, the geophysical (level 2) retrievals are reported at the nominal resolution of 40.5 km at nadir.

The AIRS retrieval algorithm makes use of a cloud-clearing technique described in detail in Susskind et al. (2003). Briefly, the technique takes advantage of the fact that while IR retrievals are strongly affected by the presence of clouds, microwave temperature retrievals are largely insensitive to the presence of clouds. Thus, any horizontal inhomogeneity in the radiances observed by the three-by-three array of IR footprints within the microwave footprint is largely caused by varying amounts of clouds within each IR FOV. One important assumption in this approach is that only the relative amount and not the radiative properties of a given cloud type vary between the IR FOVs. A second assumption is that the geophysical properties that are retrieved in the clear portions of the FOVs are identical in each IR FOV. Making use of this technique requires no *a priori* assumptions about or modeling of the cloud properties (height, emissivity, etc.), nor does it limit the IR retrievals to rare clear-sky scenes.

We use retrievals of clear sky outgoing longwave radiation ($OLR_{CS}$) and profiles of water vapor mixing ratio (w), saturation water vapor mixing ratio ($w_s$), and temperature (T) from the AIRS version 4, level 2 (swath) product. The profile of w is a layer quantity, representing the mean mixing ratio between the standard pressure levels, while profiles of $w_s$ and T are level quantities, representing the value at the pressure level. For temperatures higher than 273.15 K, $w_s$ is calculated with respect to water, otherwise it is calculated with respect to ice using the Buck (1981) formulation. We calculate the layer geometric mean $w_s$ such that the calculated RH is a layer-mean RH between pressure levels.

Atmospheric T retrievals have been compared with ECMWF analyses and dedicated radiosondes and are found to be accurate to 1°C for every 1 km thick layer (Fetzer et al. 2005). Similarly, w profiles have been compiled in 2 km layers and compared with dedicated radiosondes. At the Tropical West Pacific (TWP) site, Fetzer et al. (2005) find the following biases: -10.5% (1013-700 hPa), -0.7% (700-500 hPa), -2.3% (500-300 hPa), -16.1% (300-200 hPa), and 15.1% (200-150 hPa).

We apply all appropriate quality assurance flags to the AIRS dataset. AIRS products have a hierarchy of quality flags (Susskind et al. 2006), based on whether all steps in the retrieval algorithm are performed satisfactorily. Generally, precipitation and/or cloud fractions exceeding 80% in the AIRS fields of view cause the retrieval to fail. We perform additional quality control by removing all retrievals in which the RH with respect to liquid water (calculated using the Buck (1981) $w_s$ formulation) exceeds 100% at any layer within the retrieval. This removes spuriously high RHs while allowing for humidities that are supersaturated with respect to ice, as is frequently observed in the upper troposphere (c.f, Gettelman et al. 2006). Approximately 7% of the AIRS retrievals were removed due to supersaturation with respect to liquid water. Finally, the AIRS data are re-gridded to 1° horizontal resolution, keeping a record of the number of observations contained within each 1° box.

*b. MODIS*

The Moderate Resolution Imaging Spectroradiometer (MODIS) is a whiskbroom scanning radiometer with 36 channels between 0.415 and 14.235 μm. The retrieval of cloud properties for the level 2 products is described in detail in Platnick et al. (2003). As many as 20 channels are used in the cloud detection algorithm to create a cloud mask at 1 km resolution, which is essentially a measure of the confidence that the FOV is clear. $CO_2$ slicing within the broad 15 μm absorption band is then used to infer cloud top pressure and the effective cloud amount on a 5x5 pixel (5 km at nadir) scene, assuming at least 4 of the 25 pixels are flagged as probably cloudy or cloudy. Temperature profiles from the GDAS gridded meteorological product (Derber et al. 1991) are then used to derive cloud top temperature (CTT). Optical thickness ($\tau$) retrievals, which make use of the 0.65, 0.86, and 1.2 μm bands in addition to inferences about cloud phase, are only provided for the daytime observations (ascending orbits in the Tropics). We remove cloud retrievals that are affected by sun glint, over land, and where the cloud mask is undetermined.

Using the cloud fraction, CTT, and $\tau$ data at 5 km (nadir) resolution, we calculate histograms of average high (CTT < 245 K) cloud fraction in three bins of $\tau$ at 1° horizontal resolution as in Kubar et al. (2007). To ensure sufficient sampling for each histogram, we require that at least 65 MODIS pixels are contained within each 1° grid space (consistent with Kubar et al. (2007)). For each 1° grid space, we bin the cloud fractions based on $\tau$ ranges that are chosen to distinguish high clouds with negative radiative forcing ($\tau \geq 4$) from high thin clouds with positive radiative forcing ($\tau < 4$). The clouds with negative forcing are further separated into anvil ($4 \geq \tau < 32$) and thick ($\tau \geq 32$) clouds. The assumption here, which will be supported by the results, is that the intermediate optical depth cold cloud corresponds to extended upper level anvil cloud associated with convection, while the thick cold cloud is more closely associated with heavy precipitation.

### *c. AMSR-E*

AMSR-E is a conically-scanning passive microwave radiometer sensing polarized radiation at six frequencies between 6.9 and 89 GHz. The AMSR-E instrument and retrieval algorithms are explained in detail in Japan Aerospace Exploration Agency (2005). We use retrievals of column-integrated water vapor (WVP) over the ocean from the AMSR-E version 5 ocean product. WVP is retrieved using the 18.7, 23.8, and 36.5 GHz brightness temperatures. First, cloud liquid water index (CWI) is derived from brightness temperature, atmospheric transmittance, and vertical mean atmospheric temperature at 18.7 and 36.5 GHz. Then, WVP is calculated from the CWI, atmospheric transmittance at 18.7 and 23.8 GHz, and a set of regression coefficients which minimize differences between WVP and the precipitable water from radiosondes. These data are mapped onto a 0.25° resolution grid by Remote Sensing Systems and WVP retrievals are discarded in the presence of heavy rain. We re-grid these data to 1° resolution, keeping a record of the number of observations contained within each 1° box..

*d. TMPA*

The Tropical Rainfall Measuring Mission (TRMM) Multisatellite Precipitation Analysis (TMPA) provides precipitation rates at three hour resolution between 50°S and 50°N from a suite of polar orbiting and geostationary satellites. Huffman et al. (2007) provide a detailed description of the dataset. The data are collected from the Microwave Imager (TMI) on TRMM, Special Sensor Microwave Imager (SSM/I) on Defense Meteorological Satellite Program (DMSP) satellites, AMSR-E on Aqua, and the Advanced Microwave Sounding Unit-B (AMSU-B) on the National Oceanic and Atmospheric Administration satellite series. These polar orbiting passive microwave sensors cover about 80% of the earth's surface between 50°S and 50°N over three-hour periods. Precipitation data for the remaining 20% is inferred from window channel IR data collected by geostationary satellites. Three additional data sources are the TRMM Combined Instrument (TCI) estimate, the Global Precipitation Climatology Project

(GCPC) monthly rain gauge analysis and the Climate Assessment and Monitoring System (CAMS) monthly rain gauge analyses.

Briefly, the TMPA RR estimates are made using the following procedure: the microwave estimates are calibrated and combined, IR estimates are created using the calibrated microwave precipitation, the microwave and IR estimates are combined, and finally the rain gauge data are incorporated as a means of scaling the retrieved precipitation estimates. The data are reported at the nominal 3-hourly observation times (0000, 0300, …, 2100 UTC), averaging polar orbiting data that are ±90 minutes from these times. We make use of the version 6 3B42 product, which we re-grid from 0.25° to 1° horizontal resolution.

### *e. NCEP/NCAR Reanalysis*

Finally, 6-hourly horizontal and vertical winds from the NCEP/NCAR Reanalysis (Kalnay et al. 1996) over the same period are used. These data are linearly interpolated from 2.5° to 1° horizontal resolution and to 3-hourly resolution.

## 3. Methodology

We are interested in the moistening effects of tropical deep convection from a statistical and climatological perspective rather than from a case-by-case perspective; thus we composite over many thousands of deep convective events in the Pacific ITCZ over the three-year period Jan 2003 – Dec 2005. We locate deep convection by seeking RRs that exceed the 90$^{th}$ percentile, which – after gridding the data to 1° resolution – is 1.6 mm hr$^{-1}$ for this time period in the

Tropical Pacific (-25°N to 25°N, 120°E to 260°E). The cumulative sum of precipitation (expressed as a fraction of the total precipitation) is plotted as a function of instantaneous RR in Figure 1. During the three-year period, 57% of total rainfall in the Tropical Pacific fell in RR events that exceeded the 90$^{th}$ percentile (vertical line in Figure 1). Thus by choosing the 90$^{th}$ percentile of RR as a threshold, we concentrate on very intense convection which makes up a substantial portion of the total accumulated precipitation while still retaining a large sample size.

We composite the meteorological fields in 11x11 grids of 1° grid spaces surrounding each RR grid space exceeding this threshold value and for 24 hours before and 24 hours after the time of deep convection. Where multiple adjacent grid spaces exceed the RR threshold, the composites centered at each rainy grid space are averaged into one distinct realization so as to maintain the most conservative estimate of the number of independent samples.

Even though AQUA passes over a given location only once every 12 hours in the Tropics, the precipitation data are provided every three hours everywhere, thereby resulting in sampling of geophysical quantities at a wide range of time offsets from the deep convection events. We choose composite temporal increments of 3 hours by averaging all retrievals that fall within ±90 minutes of the three hour increments. For example, any Aqua overpass that occurred between 4.5 and 1.5 hours prior to a high RR observation is placed at hour -3.

The use of a reference frame centered on intense RRs that is fixed in time over the 48 hour period surrounding the convective events is chosen to study the effects of convection on the environment in an Eulerian sense: generally, convective systems pass through the domain from east to west within the tropical easterlies. Unlike the studies of Soden (1998, 2004) and Sherwood and Wahrlich (1999), we do not attempt to track convective systems but rather concentrate on the effects of convection on the environment through which the convection passes. Thus we sample a spectrum of convection, from events that pop up stochastically to convective systems that propagate in time.

Composite anomalies are computed by subtracting from each time lag the temporal mean of the composite-mean pattern over the 48-hour period. We refer to the fractional coverage of the anomaly as the fraction of the 11°x11° domain that is occupied by grid spaces that are greater than or equal to $e^{-1}$ of the maximum anomaly observed over the entire composite period. In the case of $OLR_{CS}$ and $\omega_{UT}$, the region is defined relative to the maximum (absolute) negative anomaly. We define the magnitude of the anomaly as the maximum positive anomaly at each time lag, except for $OLR_{CS}$ and $\omega_{UT}$, in which case the magnitude is the maximum (absolute) negative anomaly at each time lag. We choose these metrics rather than simply taking spatial averages across the domain because they retain scale and magnitude information, allowing for separation of small-scale but very anomalous features from large scale weakly anomalous features which might appear identical in spatial averages. For anomalies that are three-dimensional (e.g. RH anomalies), we first average the composite anomalies over the appropriate levels (e.g., between 500 and 200 hPa for upper tropospheric anomalies), then calculate the fractional coverage such that we are only reporting the horizontal extent of the anomalies. As will be shown below, many anomalies propagate out of the domain, so it is not always possible to say with certainty when they have spread to their largest extent or have reached their maximum amplitudes. In these cases we simply put a lower bound on the time at which these occur.

## 4. Results

Results are shown for convection observed within the tropical Pacific ITCZ, defined as 5°-15°N, 120°E-260°E. Aside from spatial pattern differences due to underlying SSTs, the results shown here are robust throughout the Tropics, assuming a climatologically convective region is chosen for analysis. Composites generated using only observations from ascending AQUA passes (1:30 pm local time) show no differences from those generated using only descending AQUA passes (1:30 am local time), nor do seasonal differences affect the results.

*a. Composites about all RRs exceeding the 90$^{th}$ percentile*

Plan views of eight composite-mean variables as a function of time relative to the high precipitation event are shown in Figure 2. As required by the compositing technique, the central grid space in the plan view at hour 0 contains the maximum RR and the composite-averaged RR is significantly lower in the hours preceding and proceeding this time. High RRs are confined to the central portion of the domain and are observed for only a few hours before and after peak RR.

Composite-mean WVP is highest near the center of the domain, with larger meridional than zonal gradients (i.e., the moist region is elongated in the east-west direction). The zonal elongation of mean WVP reflects the underlying SSTs in the analysis region, which extends from the northern edge of the western Pacific warm pool in the west to a narrow warm tongue of relatively high SSTs in the east (c.f., Figure 1 of Kubar et al. 2007).

$OLR_{CS}$ is correspondingly lower where the composite mean WVP is higher (i.e., near the center of the domain), as the bulk of the radiation escaping to space originates from a higher altitude and therefore lower temperature where it is more moist. A subtle but important difference between the $OLR_{CS}$ and WVP will become apparent in the anomaly patterns discussed below.

Composite-mean high thick cloud fraction looks nearly identical to the precipitation, maximizing at hour 0 and falling off rapidly away from hour 0, in addition to remaining confined to the center of the domain. This strengthens our confidence that the optical depth threshold chosen to define thick high clouds ($\tau \geq 32$) is indeed capturing the deep convective cores.

Whereas the high thick clouds only cover the heavily precipitating region and peak in phase with the precipitation, the anvil cloud fractions cover a larger area of the domain and peak at hour +3. The coverage of anvil clouds tends to be elongated in the zonal direction and confined in the meridional direction. This spatial pattern is mainly due to the inclusion of eastern Pacific convection, which occupies a broad range of longitudes but is confined to a relatively narrow band of latitudes over the highest SSTs (not shown). The spatial patterns and evolution of anvil cloud fraction lends credence to our choice of optical depth ranges defining anvil clouds: We expect greater spatial coverage of anvils relative to deep convective cores, as well as a time lag between peak convection and their maximum extent as they spread outward from deep convection. This result is also consistent with previous studies (Soden 2000, 2004; Tian et al. 2004) that show a time lag between the peak convective cloud fraction and the peak anvil cloud fraction.

High thin cloud is well distributed in space and time outside of where the high thick and anvil clouds are predominant. Largest high thin cloud fractions tend to be near the edge of the anvil clouds. Note that the local minimum in high thin cloud fraction near the center of the domain between hour -6 and hour +6 is simply an artifact of there being only a finite area for all three cloud types to occupy: The high thin cloud fraction must be lower to accommodate the large thick and anvil cloud fractions present near the deepest convection.

Plan-views of the anomalies calculated by subtracting from each time lag the temporal mean of the composite-mean pattern over the 48-hour period are shown in Figure 3. In addition, fractional coverages and anomaly magnitudes of these fields are plotted in Figure 4. Fractional coverage of the anomaly region refers to the fraction of grid spaces in the 11°x11° domain at each time lag that are greater than or equal to $e^{-1}$ of the maximum anomaly observed over the entire composite period. Anomaly magnitude refers to the maximum anomaly at each time lag. In the cases of $\omega_{UT}$ and $OLR_{CS}$, the quantities are calculated with respect to the maximum (absolute) negative anomaly. The errorbars represent the 95% confidence limits averaged in space over the domain.

RR anomalies look identical to composite-mean RRs because we have isolated very extreme RR events. Anomalously high RRs are confined to the central portion of the domain and peak at approximately 2 mm hr$^{-1}$ at hour 0.

Peak WVP anomalies (Figure 4d) coincide with the peak RR (Figure 4b), which is consistent with the instantaneous correlations between RR and WVP shown in Bretherton et al. (2004). Anomalies of WVP clearly show a westward propagation of a moist signature. Thus it is likely that the majority of the convection observed in these composites does not occur spontaneously but rather is organized into convective systems that propagate from east to west in time, as documented by Reed and Recker (1971). The WVP anomaly size remains essentially constant as the system crosses the domain (Figure 4c).

As alluded to above, $OLR_{CS}$ anomalies behave quite differently than WVP anomalies. Rather than peaking at hour 0, they reach maximum amplitude following the convection and are anomalously lower in the 24 hours following convection than in the 24 hours prior to convection (Figure 4d). As will be shown below, the region of reduced $OLR_{CS}$ corresponds to a sustained moist anomaly in the upper troposphere following deep convection.

Whereas anomalously high thick cloud fractions only cover the heavily precipitating region and peak in phase with the precipitation, the anvil cloud fraction anomalies cover a larger area of the domain, peak at hour +3, and remain extensive for several hours following convection (Figures 4a-b).

The region occupied by anomalously large fractions of high thin cloud (not shown) is larger at nearly all times than either high thick or anvil cloud, though the anomalies themselves are quite small (~2%). This difference would be more dramatic if the fractional coverages were calculated over a larger domain that captures the broad horizontal extent of high thin cirrus clouds.

The asymmetry in $OLR_{CS}$ anomalies in the presence of symmetric WVP anomalies can be explained by the pattern of RH anomalies, shown in Figure 5. Whereas the low-level (below 700 hPa) RH anomalies peak just prior to the maximum RR (hour 0), the upper troposphere (600 hPa - 200 hPa) is anomalously moist between 3 and 24 hours following the convection in both regions. The RH anomalies in the upper troposphere are much larger than those in the lower troposphere, peaking around 10% at hour +9 (Figure 4b). Anomalies above 200 hPa are negligible.

These results are consistent with the lag correlations between radar-derived rain rate and lower and upper tropospheric RH from radiosondes shown in Sobel et al. (2004): Lower tropospheric RH ($RH_{LT}$) is highly correlated with rain rate at lags of -6 hours and 0 hours, while peak correlation between upper tropospheric RH ($RH_{UT}$) and rain rate occurs at a lag of +6 hours. The peak correlation is stronger for $RH_{UT}$ than for $RH_{LT}$.

The fractional coverage of the $RH_{UT}$ anomaly region increases until at least hour +15 (Figure 4a). Beyond hour +18, the RR anomaly has moved out of the domain, but the residual $RH_{UT}$ anomaly near the western edge of the domain is still greater than that at the center of the domain at hour 0.

It is important to note that fractional anomalies from the composite mean mixing ratio (not shown) exhibit the same patterns and magnitudes as the RH anomalies, indicating that the positive RH anomalies at upper levels are not due to temperature changes. The temperature perturbations (not shown) are negligible (on the order of 0.1 K throughout the troposphere) and changes in RH are almost entirely due to mixing ratio changes. The absence of substantial temperature perturbations over the course of several individual convective events and over the course of a composite easterly wave was noted by both Sobel et al. (2004) and Reed and Recker (1971), respectively.

To elucidate the co-evolution of humidity and vertical motion, spatial averages across the 11°x11° domain are calculated of omega and of anomalies of omega and RH (Figure 6). Although upward motion is observed throughout the troposphere at all times in the composite period, it shifts from bottom-heavy prior to convection to top-heavy following the convection. Anomalous upward motion reaches peak amplitude in the upper troposphere at hour 0 (Figure 4b), but occupies the deepest region of the troposphere at hour -3 (Figure 6). Surprisingly, the lower troposphere is anomalously subsiding at hour 0 (Figure 6). Anomalously top-heavy vertical motion exits the domain by hour +15. Both the fractional coverage and the magnitude of the upper tropospheric vertical motion ($\omega_{UT}$) anomaly reach a broad peak around hour 0 (Figures 4a-b).

Rough calculations show that the magnitude of spatial-mean composite-anomalous ascent in the mid-troposphere is consistent with the spatial mean composite RR anomalies. Simple scaling arguments show that a 1 mm day$^{-1}$ precipitation anomaly – which is on the order of spatially-averaged RR anomalies observed in this study (not shown) – should correspond to a mid-tropospheric $\omega$ anomaly of -10 hPa day$^{-1}$. Indeed, we observe spatially-averaged $\omega$ anomalies that are approximately this magnitude, which indicates that the reanalysis is (roughly) capturing the vertical motion associated with deep convection. Poorer agreement between these quantities is observed at smaller spatial scales, as would be expected given the coarse resolution of the reanalysis compared to the scale of deep cumulonimbus updrafts.

Further consistency is evident between the evolution of the spatially-averaged vertical motion anomalies and spatially-averaged humidity anomalies shown in Figure 6c. Spatially-averaged RH anomalies clearly show a moist anomaly prior to peak convection at the low levels (below 700 hPa) followed by a significantly larger moist anomaly at upper levels after the peak convection. Roughly, moistening occurs where there is ascent (e.g., in the lower troposphere between hours -21 and -3 and in the upper troposphere between hours -12 and +12) and drying occurs where there is descent (e.g., in the upper troposphere between hours -24 and -18 and between hours +15 and +24). This is to be expected, given that the humidity tendency is proportional to the magnitude of upward motion in the presence of a strong downward gradient of absolute humidity.

The vertical motions provided on the 2.5°x2.5° reanalysis grids are unlikely to capture all small-scale motions that characterize deep convection or motions driven by local cloud radiative effects, and are largely model output rather than observations in the remote areas of the Tropical Pacific studied here. Nonetheless, the reanalysis does a remarkably good job – at least in the composite sense – of producing a vertical motion field in an environment of tropical deep convection that evolves in a similar manner to that shown in observational studies (e.g., Fig. 8 of Reed and Recker 1971, Fig. 6 of Gamache and Houze 1983, Fig. 8f of Nuret and Chong 1998) and that is consistent with humidity and precipitation anomalies observed from space.

*b. Composites as a function of spatially-averaged RR*

We now sort the composites by the spatially-averaged RR at hour 0. While still requiring that the central RR grid space at hour 0 in each composite exceeds the 90$^{th}$ percentile, the composites are now stratified by the average RR over the entire domain. This separates large systems with heavy precipitation occurring over broad regions from small systems that are more confined in space. We refer to the lowest (highest) quartile of spatially-averaged RR as the low (high) RR regime. For consistency, the anomaly regions are calculated with respect to the maximum anomalies observed using all observations (i.e., the maxima from the unsorted results discussed above rather than the maxima within each RR regime). Figures 7-9 show fractional coverage and magnitude of anomalies of RR, WVP, $OLR_{CS}$, high thick, anvil, and thin cloud fraction, $\omega_{UT}$, and $RH_{UT}$ for each RR regime, along with the results using all observations (i.e., the unsorted results shown in Figure 4). In general, the composite anomaly plan views (not shown) have similar patterns to those generated using all observations (Figures 3 and 5), but the size and amplitude of the anomalies tends to increase with spatially-averaged RR.

Anomalously high RRs cover the greatest fraction of the domain at hour 0 in all regimes, with fractional coverage increasing with RR regime (Figure 7a). Because the scale of the convective system increases with RR regime, the anomalous RR region arrives in the domain earlier and exits later with increasing RR regime. The anomaly amplitudes (Figure 7b) are indistinguishable among RR regimes at hour 0 because the composites are all centered on RRs exceeding the 90$^{th}$ percentile. Thus sorting by spatially-averaged RR at hour 0 tends to separate large systems (4$^{th}$ quartile) from small systems (1$^{st}$ quartile).

The size of the region occupied by WVP anomalies remains essentially constant at about 10% across the composite period in all RR regimes (Figure 7c). Though the WVP anomaly peaks at hour 0 in all regimes, the anomaly amplitude is larger in the lower RR regimes (Figure 7d). This is consistent with the relationship between instantaneous RR and absolute WVP derived in Bretherton et al. (2004). An implication of the relationship is that a larger WVP anomaly is required in a relatively dry environment (lower RR regime) compared to a relatively moist environment (higher RR regime) to produce the same RR anomaly, as is the case here. Again, the symmetry of WVP anomaly amplitude about hour 0 can be contrasted with the $OLR_{CS}$ anomaly (Figure 7f).

The fractional coverage of the $OLR_{CS}$ anomaly increases from just prior to convection until reaching peak coverage following convection (Figure 7e). The anomalies are generally greater and more expansive for the high RR regimes and reach maximum size at the same time as the corresponding $RH_{UT}$ anomalies (discussed below). Maximum (absolute) $OLR_{CS}$ anomalies between -5 and -9 W m$^{-2}$ are observed at hour +3 in all RR regimes (Figure 7f), but the fractional coverage tends to remain expansive until at least hour +12 in all RR regimes.

The fractional coverage and anomaly magnitude of high thick cloud fraction evolves in a nearly identical manner to RR anomalies, though the fractional coverage is much smaller (Figure 8a). Similar to the RR anomalies, high thick cloud fraction anomalies grow rapidly to a peak at hour 0 and then rapidly decrease (Figure 8b). The fractional coverage is likewise stratified by RR regime, with thick cloud occupying a larger portion of the domain throughout the composite period in the higher RR regimes. Plan views of thick cloud fraction anomalies show that the anomaly region expands zonally and becomes more persistent with RR regime (not shown).

The evolution of anvil cloud fraction anomalies is quite different from those of RR and deep convective cloud. Anomalously high anvil cloud fractions reach their maximum extent and maximum amplitude at hour +3 in all RR regimes (Figures 8c-d). After hour +3, the anomaly magnitude tends to be slightly greater in the higher RR regimes. The fractional size of the domain in which anvil cloud fractions are anomalously high is greater for higher RRs at all times in the composite. Thus deep convection that occupies a larger area of the domain results in broader anvil cloud coverage, though peak coverage consistently occurs at hour +3 across the regimes.

Because of the spatial and temporal ubiquity of high thin clouds throughout the composite period and throughout the composite domain, high thin cloud fraction anomalies are small (Figure 8f) and changes in their fractional coverage (Figure 8e) largely reflect changes in the coverage of high thick and anvil cloud fractions.

Between hour 0 and hour 6, the fractional coverages of the $RH_{UT}$ anomalies in the four regimes are virtually indistinguishable (Figure 9a). Between hour +6 and hour +15, the moist anomaly in the low RR regime tends to maintain its size, covering approximately 10% of the domain, while the anomalies in the other regimes continue to spread until at least hour +15.

Anomaly size increases with spatial-averaged RR, with the second, third, and fourth RR quartiles having $RH_{UT}$ anomalies that occupy approximately 25%, 50%, and 70% of the domain, respectively, at their peak extents. The region of anomalously high $RH_{UT}$ remains extensive for the remainder of the composite period in all regimes. Clearly, deep convection is pumping moisture into the upper troposphere over a larger scale in the higher RR regimes throughout the composite period. In the lower RR regimes, the convection is occurring on a smaller scale and so the upper tropospheric moistening is confined to the center of the domain (not shown).

The $RH_{UT}$ anomaly amplitudes peak at hour +9 in the lowest three RR quartiles and at hour +12 in the $4^{th}$ RR quartile (Figure 9b). After hour +9, the $RH_{UT}$ anomalies are clearly stratified by RR regime, with larger anomalies in higher RR regimes. Thus both the size and amplitude of moist anomalies increase with the size and amplitude of convection. It is important to recall that the anomalies are calculated individually for each regime with respect to the mean over their respective composite periods. Both the composite-mean $RH_{UT}$ (not shown) and the maximum $RH_{UT}$ anomaly are greater in the higher RR regimes than the lower RR regimes. It is interesting to note that $RH_{UT}$ anomalies always peak several hours after the peak anvil extent.

The $\omega_{UT}$ anomalies (Figure 9c-d) are likewise stratified by the RR regime, with high RR regimes characterized by largest $\omega_{UT}$ anomalies (in both extent and magnitude). $\omega_{UT}$ anomalies in the low RR regime are essentially zero, indicating that the reanalysis is not capturing the updrafts that characterize deep convection on scales smaller than about 250 km (the resolution of the reanalysis). The spatial extent of $\omega_{UT}$ anomalies exhibits a broad peak between hour -9 and hour +9 (except in the lowest quartile, where no $\omega_{UT}$ anomalies exist) and is larger for larger RR regimes. In all but the lowest RR regime, the anomalous ascent covers a large portion of the domain between hour -12 and hour +12. Upper tropospheric ascent peaks at hour 0 in all RR regimes (except RR quartile 1). It should also be noted that all RR regimes except the 1st quartile show evidence of an upward propagating ω anomaly over the composite period (not shown).

## 5. Conclusions

In addition to its importance for the tropical mean circulation, deep convection is the main mechanism for vertically redistributing clouds and humidity throughout the Tropics. This latter virtue is of critical importance for the energy balance of the entire planet, and serves as a fundamental link between discrete mesoscale atmospheric processes and the Earth's climate. Making observations of these small scale processes in great detail in a range of locations is absolutely necessary for better understanding the Earth's climate and using this information to model climate change. The analysis herein has illustrated a means of studying the complex interactions of precipitation, clouds, humidity, radiation, and dynamics at relatively fine spatial and temporal scales, and can be extended over the entire globe.

In this study, a compositing technique centered in space and time on locations in the Pacific ITCZ experiencing intense precipitation was used to investigate the response of clouds, humidity, clear-sky OLR, and vertical motion to tropical deep convection. Nearly 60% of the total precipitation in the Tropical Pacific falls in events upon which these composites are based. Moistening occurs at low levels prior to convection and in the upper troposphere for several hours following convection. The magnitude of the RH anomaly at upper levels is much greater than that at low levels, and spreads outward for at least 15 hours to cover a much larger region than that occupied by the precipitation anomaly. Whereas thick convective cloud fractions peak at the time of the intense precipitation event, anvil clouds spread outward from the convective region in time, reaching maximum spatial extent three hours later. Although the domain-averaged column integrated water vapor remains essentially constant over the composite period, $OLR_{CS}$ is significantly lower following convection, highlighting its sensitivity to the coincident upper tropospheric moist anomaly. Large-scale vertical motion is upward throughout the troposphere during the composite period, but anomalous ascent shifts from the lower troposphere to the upper troposphere over the course of the convection. This transition from bottom-heavy to top-heavy vertical motion is consistent with previous observational studies of tropical convection and nicely corresponds to the pattern of moistening observed here.

Broader regions of anomalously high RRs tend to be associated with larger anvil cloud fraction, $OLR_{CS}$, $RH_{UT}$, and $\omega_{UT}$ anomalies, as is shown by sorting the composites by the spatially-averaged RR at the time of peak convection. The temporal evolution of the anomalies is consistent across all spatial scales of intense convection, however. Additionally, the results shown here are consistent throughout the convective Tropics for all seasons, regardless of whether the observations come from the ascending or descending AQUA orbit.

Tropical convection is organized on a broad range of spatio-temporal scales. An interesting extension of the analysis presented in this work would be to investigate the similarity of the results shown here to those at larger spatial and longer temporal scales. For example, does the persistence in upper tropospheric humidity anomalies following precipitation anomalies also exist at larger spatial and temporal scales? If so, how does this shape our understanding of Tropical deep convection and its role in climate, and what can this tell us about interactions at various scales?

**Acknowledgements**

The work presented in this paper was supported by a NASA Earth and Space Science Fellowship and NASA EOS Grant NNG05GA19G. We thank Chris Bretherton and Rob Wood for their helpful comments and suggestions on this work. AIRS data are distributed by the AIRS Data Services branch of the Goddard Earth Sciences Distributed Active Archive Center (DAAC), Goddard Space Flight Center (GSCF), Greenbelt, Maryland. MODIS data are distributed by the Level 1 and Atmosphere Archive and Distribution System (LAADS), Goddard Space Flight Center, Greenbelt Maryland. AMSR-E data are provided by Remote Sensing Systems and sponsored by the NASA Earth Science REASoN DISCOVER Project and the AMSR-E Science Team. TMPA data are distributed by the Goddard Earth Sciences Distributed Active Archive Center (DAAC), Goddard Space Flight Center (GSCF), Greenbelt, Maryland. NCEP/NCAR Reanalysis data provided by the NOAA/OAR/ESRL PSD, Boulder, Colorado, USA.

**References**

Allan, R.P., K.P. Shine, A. Slingo, and J.A. Pamment, 1999: The dependence of clear-sky outgoing longwave radiation on surface temperature and relative humidity. *Q.J.R. Meteorol. Soc.*, **125**, 2103-2126.

Aumann, H.H., M.T. Chahine, C. Gautier, M.D. Goldberg, E. Kalnay, L.M. McMillin, H. Revercomb, P.W. Rosencranz, W.L. Smith, D.H. Staelin, L.L. Strow, and J. Susskind, 2003: AIRS/AMSU/HSB on the Aqua mission: Design, science objectives, data products, and processing systems. *IEEE Trans. Geosci. Remote Sens.*, **41**, 253-264.

Bretherton, C.S., M.E. Peters, and L.E. Back, 2004: Relationships between water vapor path and precipitation over the tropical oceans. *J.Clim.*, **17**, 1517-1528.

Buck, A.L., 1981: New equations for computing vapor pressure and enhancement factor. *J. Appl. Met.*, **20**, 1527-1532.

Chen, S. S., and R. A. Houze, Jr., 1997: Diurnal variation and life cycle of deep convective systems over the tropical Pacific warm pool. *Quart. J. Roy. Meteor. Soc.,* **123**, 357-388.

Colman, R.A., 2001: On the vertical extent of atmospheric feedbacks. *Clim. Dyn.*, **17**, 391-405.

Derber, J.C, D.F. Parrish, and S.J. Lord, 1991: The new global operational analysis system at the National Meteorological Center. *Wea. Forecasting*, **6**, 538-547.

Dessler, A.E. and S.C. Sherwood, 2000: Simulations of tropical upper tropospheric humidity. *J. Geophys. Res.*, **105**, 20155-20163.

Fetzer, E.J., A. Elderling, E.F. Fishbein, T. Hearty, W.F. Irion, and B. Kahn, 2005: Validation of AIRS/AMSU/HSB core products for data release version 4.0. JPL D-31448.

Gamache, J.F. and R.A. Houze, Jr., 1983: Water budget of a mesoscale convective system in the Tropics. *J. Atm. Sci.*, **40**, 1835-1850.

Gautier, C., Y. Shiren, and M.D. Hofstadter, 2003: AIRS Vis/Near IR instrument. *IEEE Trans. Geosci. Remote Sensing*, **41**, pp. 330-342.

Gettelman, A., E.J. Fetzer, A. Eldering, and F.W. Irion, 2006: The global distribution of supersaturation in the upper troposphere from the Atmospheric Infrared Sounder. *J. Climate*, **19**, 6089-6103.

Hartmann, D.L., L.A. Moy, Q. Fu, 2001: Tropical convection and the energy balance at the top of the atmosphere. *J. Climate*, **14**, 4495-4511.

Held, I.M. and B.J. Soden, 2000: Water vapor feedback and global warming. *Annu. Rev. Energy Environ.* **25**, 441-475.

Houze, R. A., Jr., 1982: Cloud clusters and large-scale vertical motions in the Tropics. *J. Meteor. Soc. Japan,* **60**, 396-410.

Houze, R. A., Jr., and A. K. Betts, 1981: Convection in GATE. *Rev. Geophys. Space Phys*., **19**, 541-576.

Huffman, G.J., R.F. Adler, D.T. Bolvin, G. Gu, E.J. Nelkin, K.P. Bowman, Y. Hong, E.F. Stocker, and D.B. Wolfe, 2007: The TRMM Multisatellite Precipitation Analysis (TMPA): Quasi-global, multiyear, combined sensor precipitation estimates at fine scales. *J.Hydrometeor*, **8**, 38-55.

Inamdar, A.K. and V. Ramanathan, 1994: Physics of greenhouse effect and convection in warm oceans. *J. Climate*, **7**, 715-731.

Japan Aerospace Exploration Agency, 2005: AMSR-E data users handbook 3rd edition.

Kalnay, E., and Coauthors, 1996: The NCEP/NCAR 40-Year reanalysis project. *Bull. Amer. Meteor. Soc.*, **77**, 437-470.

Kubar, T.L., D.L. Hartmann, and R. Wood, 2007: Radiative and convective driving of tropical high clouds. *J. Climate,* **20**, 5510-5526.

Nuret, M. and M. Chong, 1998: Characteristics of heat and moisture budgets of a mesoscale convective system observed during TOGA-COARE. *Q.J.R. Meteorol. Soc.*, **124**, 1163-1181.

Pierrehumbert, R.T., 1995: Thermostats, radiator fins, and the local runaway greenhouse. *J. Atm. Sci.*, **52**, 1784-1806.

Pierrehumbert, R.T. and R. Roca, 1998: Evidence for control of Atlantic subtropical humidity by large-scale advection. *Geophys. Res. Lett.*, **25**, 4537-4540.

Platnick, S., M.D. King, S.A. Ackerman, W.P. Menzel, B.A. Baum, J.C. Riedi, and R.A. Frey, 2003: The MODIS cloud products: algorithms and examples from TERRA. *IEEE Trans. Geosci. Remote Sensing*, **41**, 459-473.

Reed, R.J. and E.E. Recker, 1971: Structure and properties of synoptic-scale wave disturbances in the equatorial Western Pacific. *J. Atm. Sci.*, **28**, 1117-1133.

Salathe, E.P. and D.L. Hartmann, 1997: A trajectory analysis of tropical upper-tropospheric moisture and convection. *J. Climate*, **10**, 2533-2547.

Sherwood, S.C. and R. Wahrlick, 1999: Observed evolution of tropical deep convective events and their environment. *Mon. Wea. Rev.*, **127**, 1777-1795.

Shine, K.P. and A. Sinha, 1991: Sensitivity of the Earth's climate to height-dependent changes in the water vapour mixing ratio. *Nature*, **354**, 382-384.

Sobel, A.D., S.E. Yuter, C.S. Bretherton, and G.N. Kiladis, 2004: Large-scale meteorology and deep convection during TRMM KWAJEX. *Mon. Wea. Rev.*, **132**, 422-444.

Soden, B.J., 1998: Tracking upper tropospheric water vapor radiances: A satellite perspective. *J. Geophys. Res.*, **103**, 17069-17081.

Soden, B.J., 2000: The diurnal cycle of convection, clouds, and water vapor in the tropical upper troposphere. *Geophys. Res. Lett.*, **27**, 2173-2176.

Soden, B.J., 2004: The impact of tropical convection and cirrus on upper tropospheric humidity: A Lagrangian analysis of satellite measurements. *Geophys. Res. Lett.*, **31**, L20104, doi: 10.1029/2004GL020980.

Soden, B.J. and R.Fu, 1995: A satellite analysis of deep convection, upper-tropospheric humidity, and the greenhouse effect. *J. Climate*, **8**, 2333-2351.

Spencer, R.W. and W.D. Braswell, 1996: How dry is the tropical free troposphere? Implications for global warming theory. *Bull. Amer. Meteor. Soc.*, **78** (6), 1097-1106.

Susskind, J., C.D. Barnet, and J.M. Blaisdell, 2003: Retrieval of atmospheric and surface parameters from AIRS/AMSU/HSB data in the presence of clouds. *IEEE Trans. Geosci. Remote Sensing*, **41**, 390-409.

Susskind, J., C. Barnet, J. Blaisdell, L. Iredell, F. Keita, L. Kouvaris, G. Molnar, and M. Chahine, 2006: Accuracy of geophysical parameters derived from Atmospheric Infrared Sounder/Advanced Microwave Sounding Unit as a function of fractional cloud cover. *J. Geophys. Res.*, **111**, D09S17, doi:10.1029/2005JD006272.

Tian, B., B.J. Soden, and X. Wu, 2004: Diurnal cycle of convection, clouds, and water vapor in the tropical upper troposphere: satellites versus a general circulation model. *J. Geophys. Res.*, **109**, D10101, doi:10.1029/2003JD004117.

Udelhofen, P.M. and D.L. Hartmann, 1995: Influence of tropical cloud systems on the relative humidity in the upper troposphere. *J. Geophys. Res.*, **100** (D4), 7423-7440.

Yanai, M., S.Esbensen, and J-H. Chu, 1973: Determination of bulk properties of tropical cloud clusters from large-scale heat and moisture budgets. *J. Atmos. Sci.*, **30**, 611-627.

**List of Figures**

Figure 5. Plan views of anomalies of RH (%), plotted as a function of pressure between 1000 hPa and 150 hPa. Each domain is 11°x11°, centered on a RR grid space exceeding the 90$^{th}$ percentile of RR at hour 0, as described in the text. Note that the anomalies are calculated with respect to the temporal mean of the composite mean pattern over the entire 48 hour period, though only a 36 hour subset is shown.

Figure 6. Spatial averages over the 11°x11° domain of (a) composite-mean ω, (b) ω anomalies, and (c) RH anomalies. The thick solid line is the zero contour.

Figure 7. (Left column) Fractional coverage and (right column) magnitude of (top row) RR, (middle row) WVP, and (bottom row) $OLR_{CS}$ anomalies for composites in each quartile of spatially-averaged RR. The thick solid line shows the fractional coverage and amplitude of these quantities for all composites centered on RRs exceeding the 90$^{th}$ percentile. Error bars represent the 95% confidence intervals. Note that the sign of the $OLR_{CS}$ anomaly magnitude is reversed for the purposes of comparison and that the y-axes are different among the anomaly magnitudes.

Figure 8. Same as in Figure 7, but for (top row) high thick, (middle row) anvil, and (bottom row) thin cloud fraction anomalies. Note that the y-axes are different for each row.

Figure 9. Same as in Figure 7, but for (top row) $RH_{UT}$ and (bottom row) $\omega_{UT}$ anomalies. Note that the sign of the $\omega_{UT}$ anomaly magnitude is reversed for the purposes of comparison.

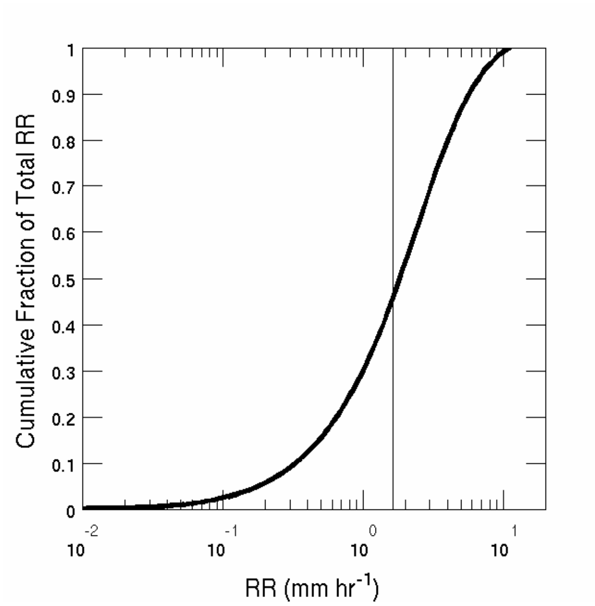


Figure 1. Fraction of total RR in the Tropical Pacific over the period Jan 2003-Dec 2005 that falls in events with instantaneous RRs less than those reported along the x-axis. The vertical line denotes the 90th percentile of instantaneous RR: 1.6 mm hr$^{-1}$. Note that the x-axis is logarithmic.

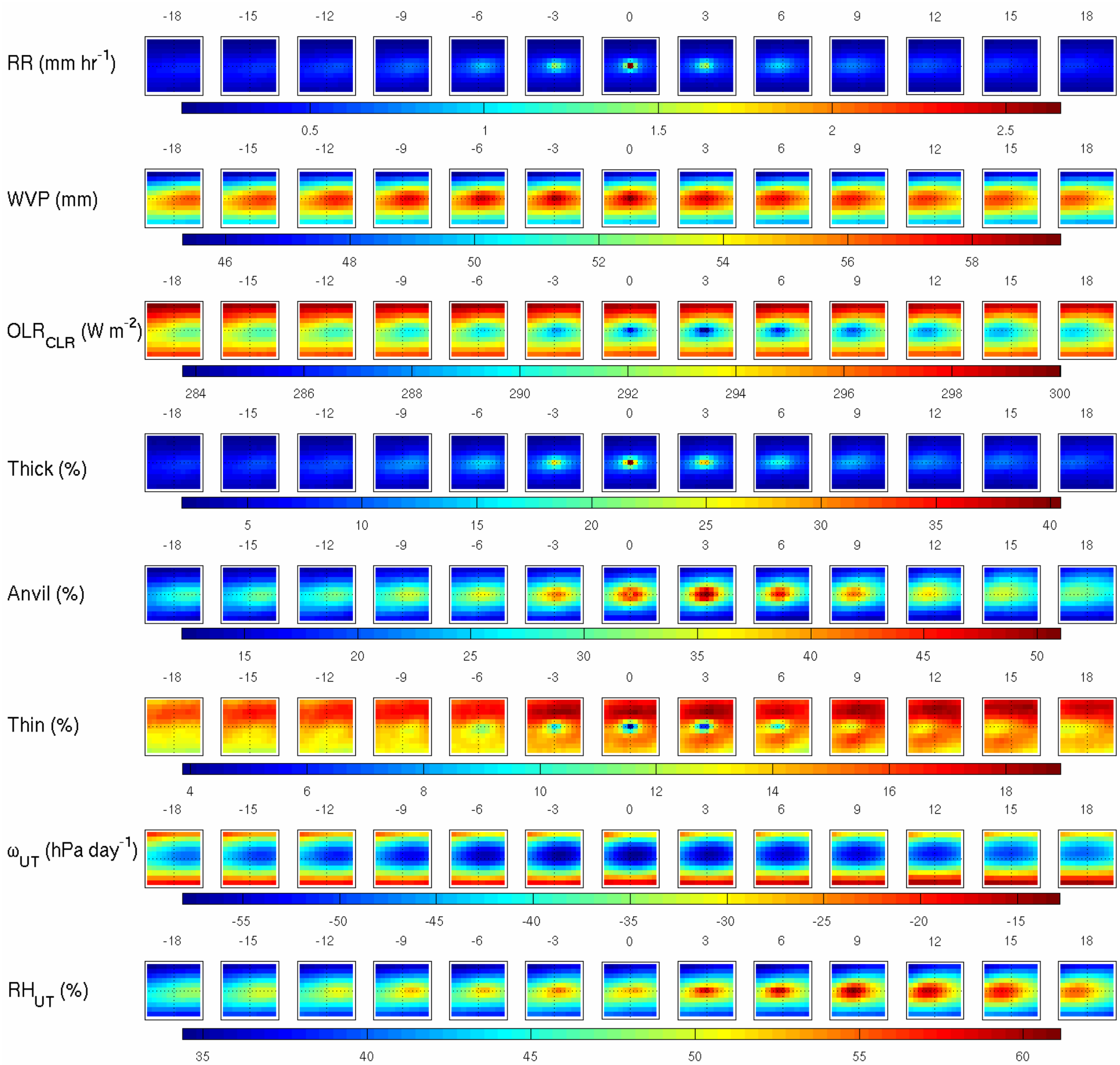


Figure 2. Plan views of composite-mean RR, WVP, OLR$_{CS}$, high thick, anvil, and thin cloud fractions, $\omega_{UT}$, and RH$_{UT}$. Note that the color scale varies among the quantities, including the cloud types. Time lags (in hours from the time of deepest convection) are shown at the top of each plan view. Each domain is 11°x11°, centered on the RR grid space exceeding the 90$^{th}$ percentile of RR at hour 0, as described in the text.

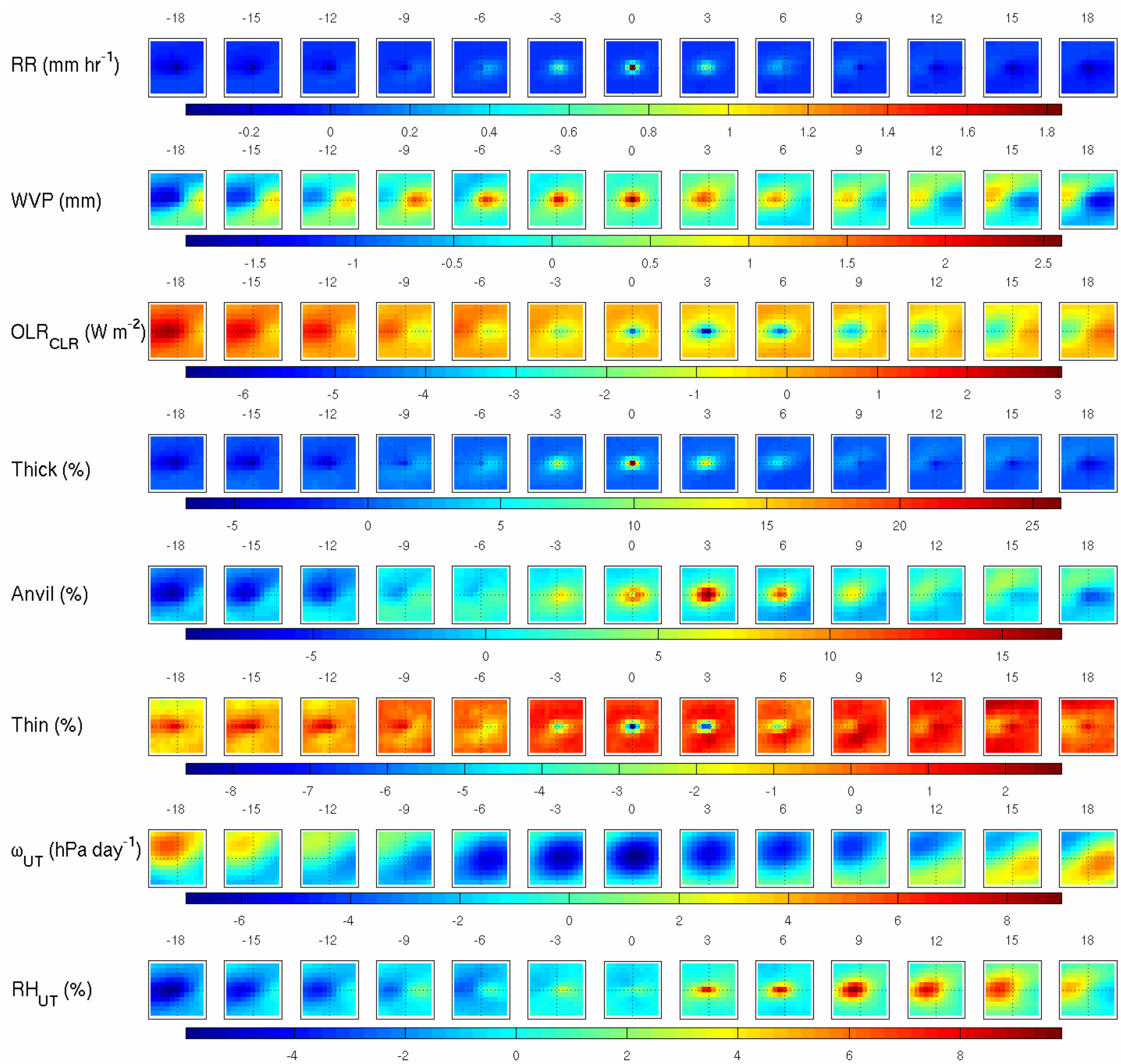


Figure 3. Same as in Figure 2, but for the anomalies from the composite mean. Note that the anomalies are calculated with respect to the temporal mean of the composite mean pattern over the entire 48 hour period, though only a 36 hour subset is shown.

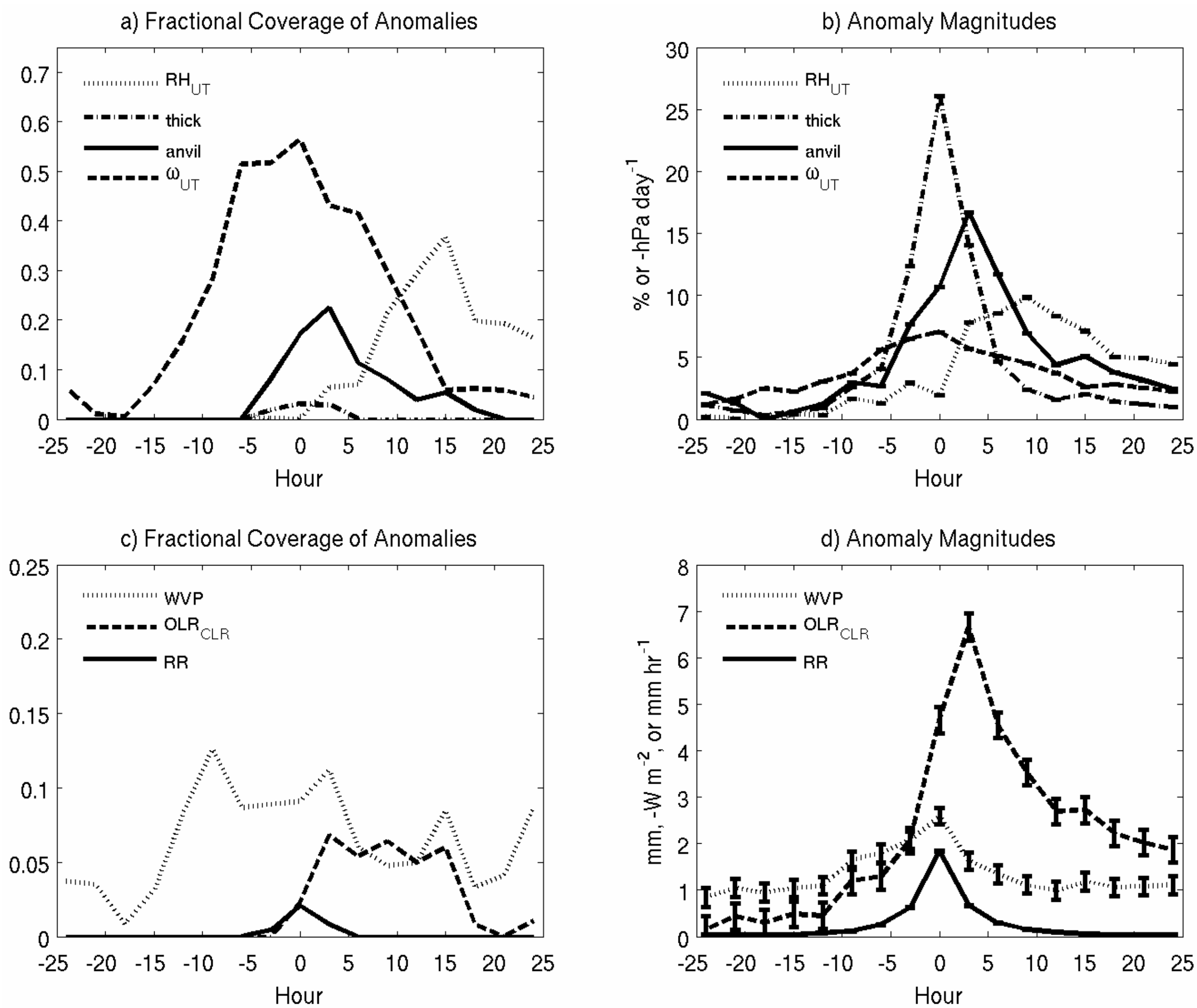


Figure 4. (Left column) Fractional coverage and (right column) magnitude of (top row) $RH_{UT}$, thick and anvil cloud fraction, $\omega_{UT}$, (bottom row) WVP, $OLR_{CS}$, and RR anomalies. Note that the amplitudes of $\omega_{UT}$ and $OLR_{CS}$ anomalies are plotted with reversed sign for the purposes of comparison and that the y-axes are different on the top and bottom rows. Error bars represent the 95% confidence intervals.

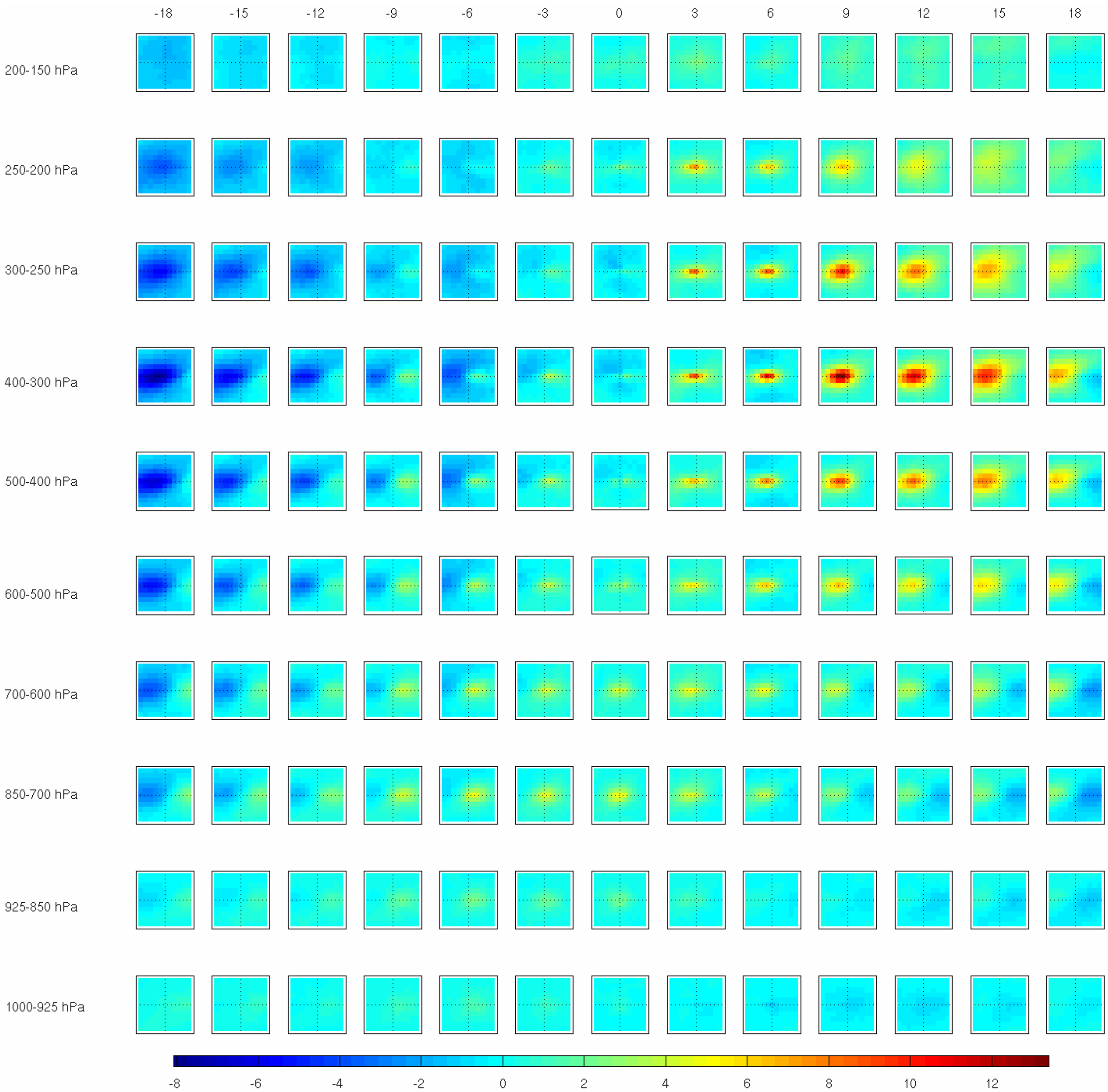


Figure 5. Plan views of anomalies of RH (%), plotted as a function of pressure between 1000 hPa and 150 hPa. Each domain is 11°x11°, centered on a RR grid space exceeding the 90th percentile of RR at hour 0, as described in the text. Note that the anomalies are calculated with respect to the temporal mean of the composite mean pattern over the entire 48 hour period, though only a 36 hour subset is shown.

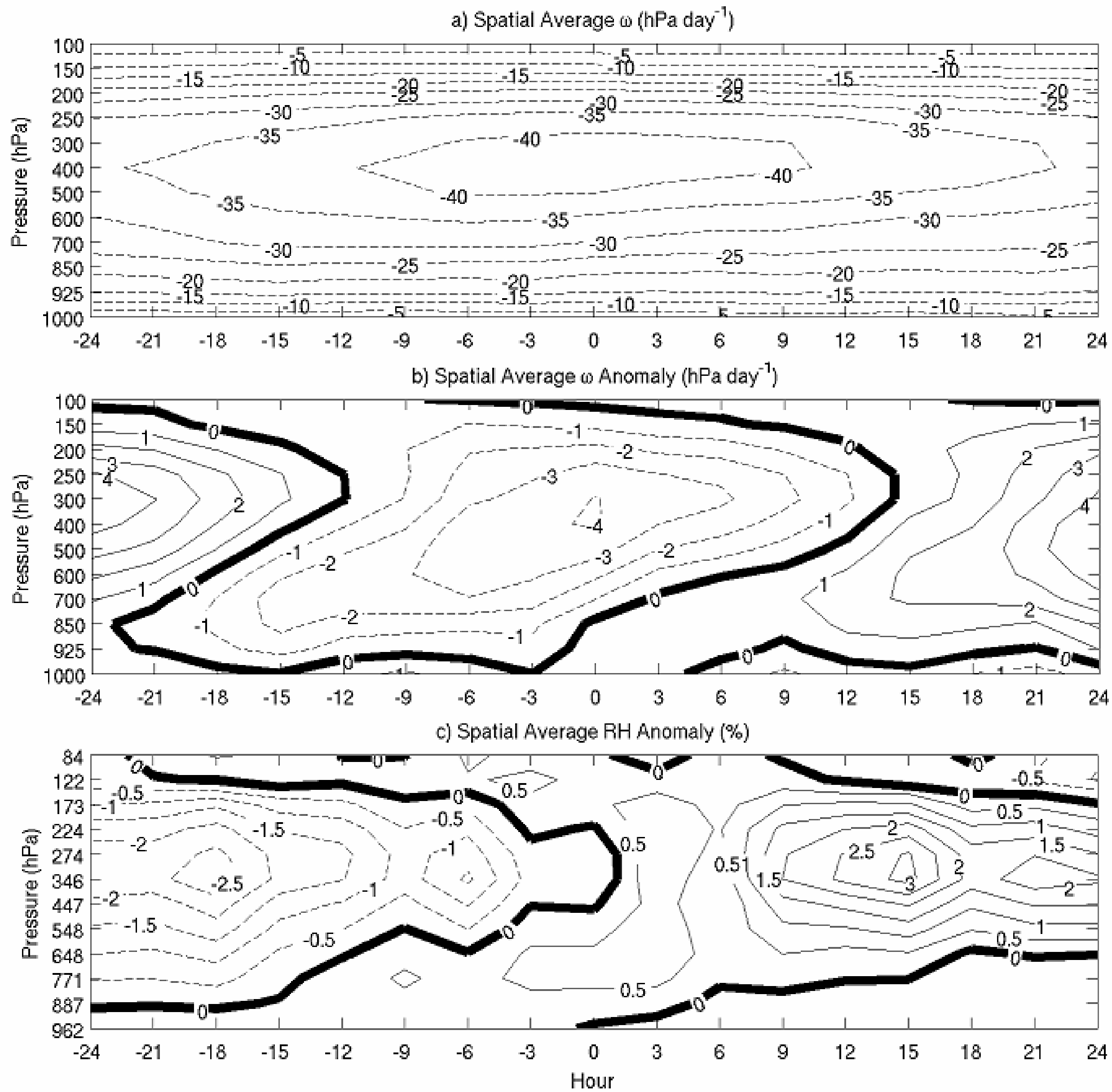


Figure 6. Spatial averages over the 11°x11° domain of (a) composite-mean ω, (b) ω anomalies, and (c) RH anomalies. The thick solid line is the zero contour.

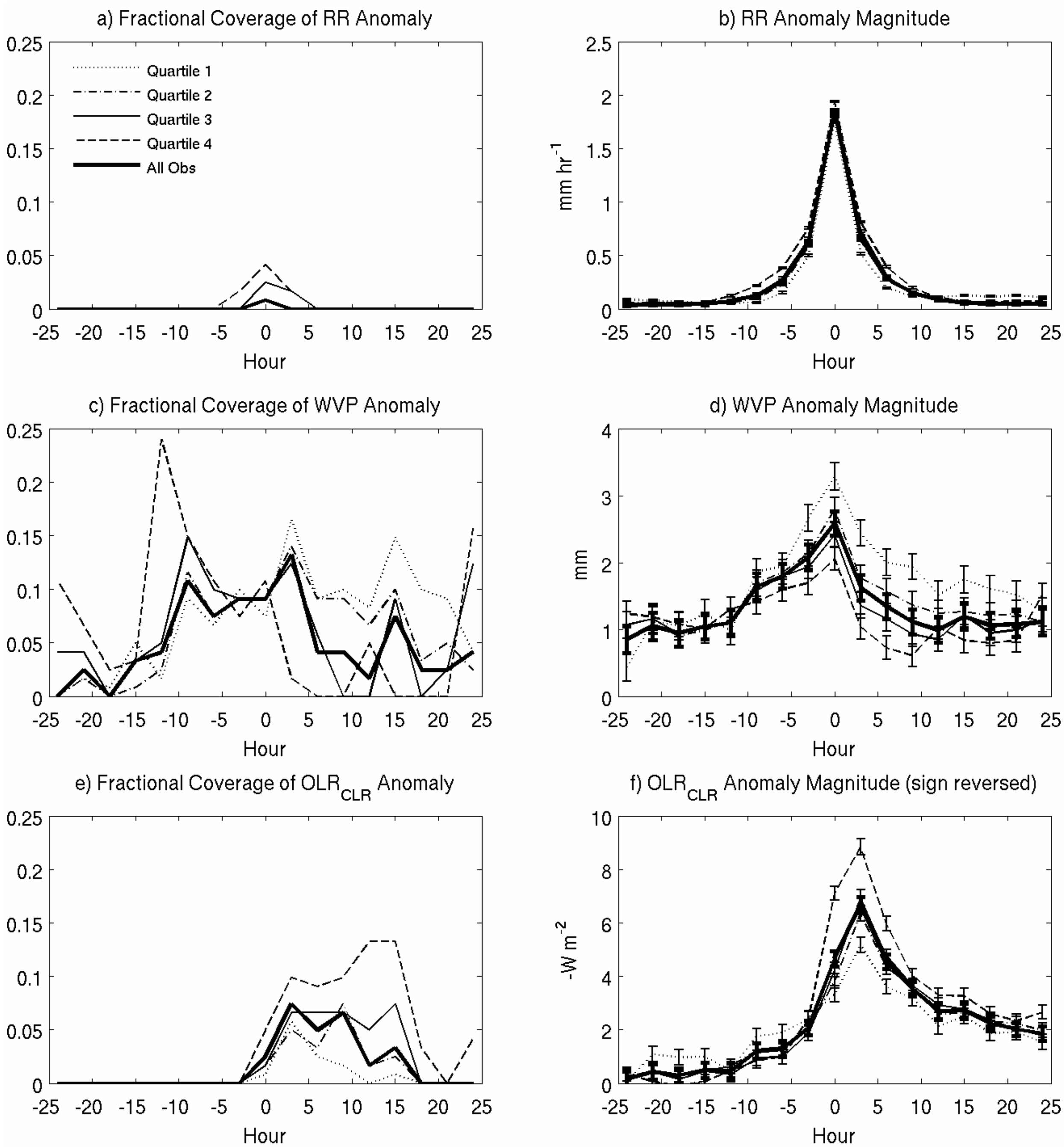


Figure 7. (Left column) Fractional coverage and (right column) magnitude of (top row) RR, (middle row) WVP, and (bottom row) $OLR_{CS}$ anomalies for composites in each quartile of spatially-averaged RR. The thick solid line shows the fractional coverage and amplitude of these quantities for all composites centered on RRs exceeding the 90$^{th}$ percentile. Error bars represent the 95% confidence intervals. Note that the sign of the $OLR_{CS}$ anomaly magnitude is reversed for the purposes of comparison and that the y-axes are different among the anomaly magnitudes.

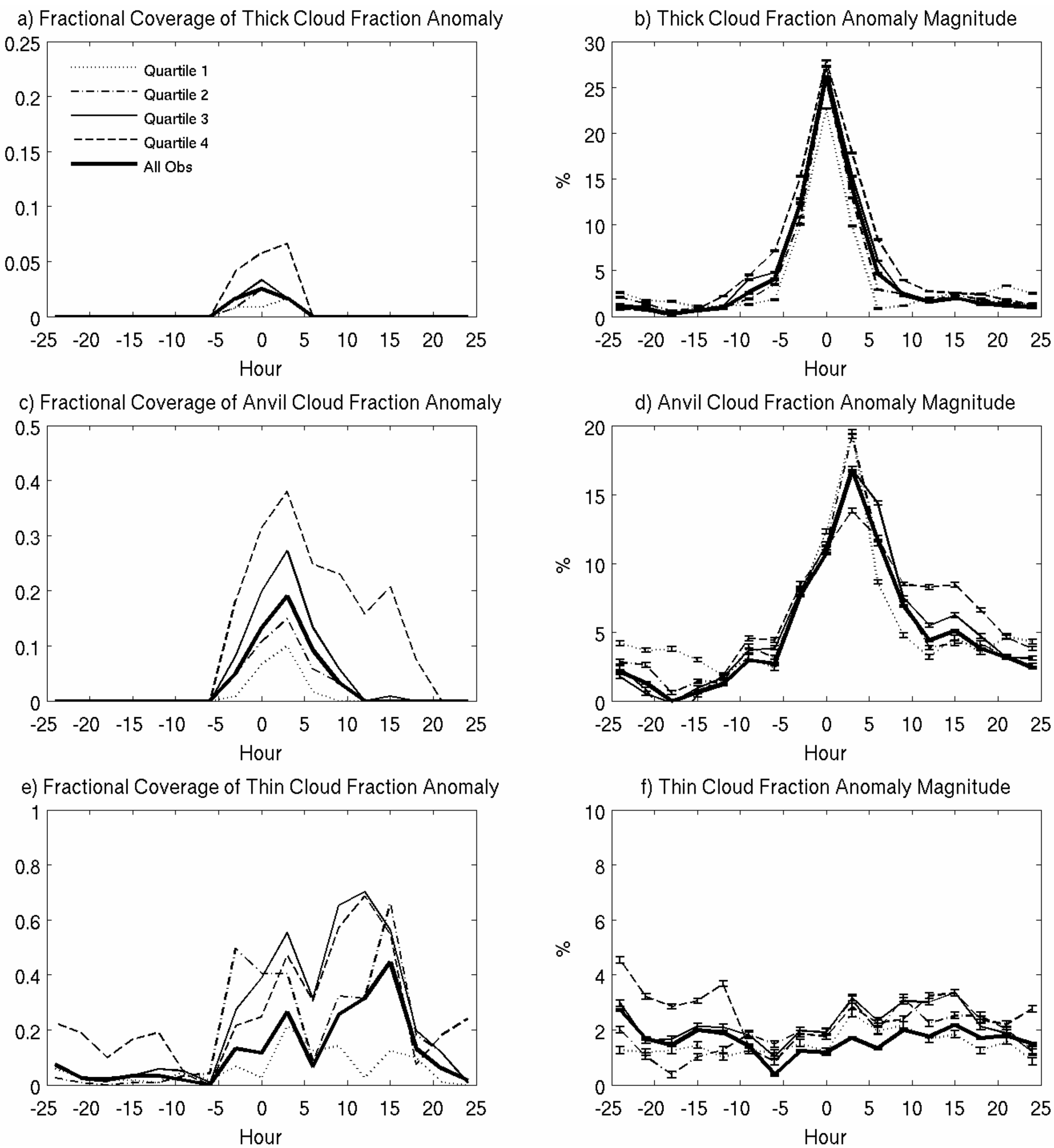


Figure 8. Same as in Figure 7, but for (top row) high thick, (middle row) anvil, and (bottom row) thin cloud fraction anomalies. Note that the y-axes are different for each row.

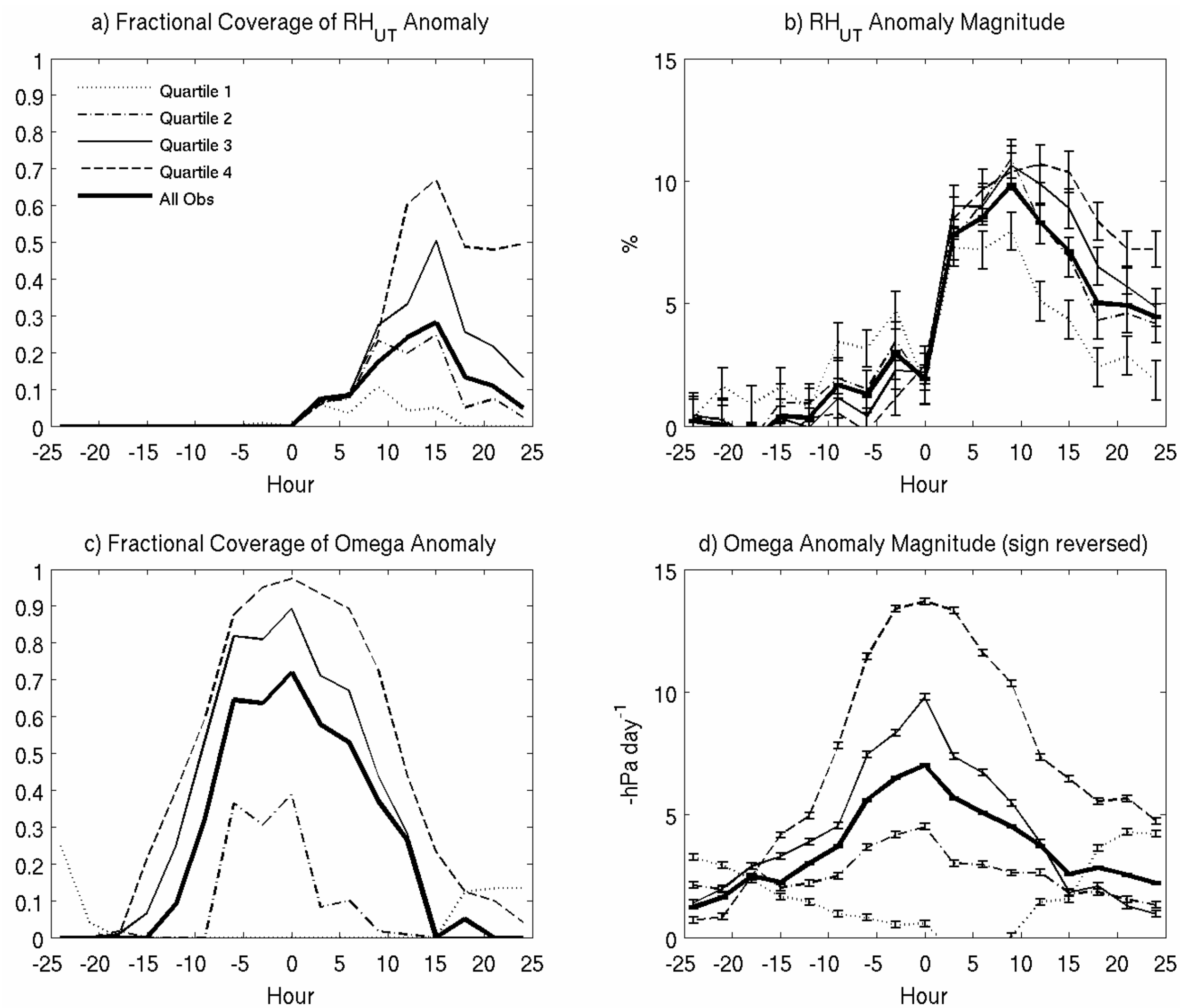


Figure 9. Same as in Figure 7, but for (top row) $RH_{UT}$ and (bottom row) $\omega_{UT}$ anomalies. Note that the sign of the $\omega_{UT}$ anomaly magnitude is reversed for the purposes of comparison.